RSC Advances

This is an *Accepted Manuscript*, which has been through the Royal Society of Chemistry peer review process and has been accepted for publication.

Accepted Manuscripts are published online shortly after acceptance, before technical editing, formatting and proof reading. Using this free service, authors can make their results available to the community, in citable form, before we publish the edited article. This *Accepted Manuscript* will be replaced by the edited, formatted and paginated article as soon as this is available.

You can find more information about *Accepted Manuscripts* in the **Information for Authors**.

ROYAL SOCIETY
OF **CHEMISTRY**

www.rsc.org/advances

1   **Synergetic effect of functionalized carbon nanotubes on ZnCr- mixed metal oxides**

2   **for enhanced solar light-driven photocatalytic performance**

3

4   Yajie Zhu [a, b], Pingxiao Wu [a, b, c,]*, Shanshan Yang [a, b], Yonghong Lu [a, b], Wen Li [a, b],

5   Nengwu Zhu [a, c], Zhi Dang [a, b], Ziyan Huang [a, b]

6   [a] *College of Environment and Energy, South China University of Technology, Guangzhou*

7   *510006, China*

8   [b] *The Key Lab of Pollution Control and Ecosystem Restoration in Industry Clusters,*

9   *Ministry of Education, Guangzhou 510006, China*

10   [c] *Guangdong Environmental Protection Key Laboratory of Solid Waste Treatment and*

11   *Recycling, Guangzhou 510006, China*

12

13   [*]Corresponding Author

14   Phone: +86-20-39380538;

15   Fax: +86-20-39383725;

16   E-mail address: *pppxwu@scut.edu.cn*

17

18

19   **Abstract:** In this work, ZnCr- mixed metal oxides (MMO) hybridized with functionalized

20   carbon nanotubes (A-CNTs) have been successfully fabricated via vacuum calcination of

21   the layered double hydroxide precursors. The structural and morphological

22   characterizations of the samples were investigated by multiple techniques such as XRD,

23   SEM, TEM, XPS, BET, Raman and UV-vis DRS. The results showed that A-CNTs were

24   well incorporated into the MMO nanoparticles to form a nanohybrid structure dependent

25   upon intimate interfacial contact. As compared to pristine MMO, the obtained

26   MMO-CNTs nanohybrids exhibited significantly enhanced photocatalytic performance for

27   bisphenol A (BPA) degradation under simulative solar light irradiation, providing powerful

28   evidence for the superiority of the hybridization with A-CNTs. The key role of A-CNTs

29   played in enhancing the photocatalytic activity of the nanohybrids was probably ascribed

30   to the larger surface area, higher visible light absorption and the more efficient restriction

31   of charge carriers recombination.

32   **Keywords:** photocatalysis; nanohybrids; mixed metal oxides; carbon nanotubes;

33   interfacial charge transfer.

34   **1. Introduction**

35   Over the past decades, increasing endeavors has been focused on semiconductor

36   based heterogeneous photocatalysis for environmental remediation and photon energy

37   conversion [1, 2]. Particularly, searching for visible-light-induced semiconductors with

38   excellent photocatalytic efficiency and physicochemical stability is critical to the practical

39   application of photocatalysis. To date, heterogeneous photocatalysis assisted by common

40   metal oxides such as ZnO, TiO_2 and their derivatives has proven to be an efficient and

41   acceptable method for the purification of organic pollutants in aqueous phase [3-8].

42   However, the wide band gap ($E_g > 3.0$ eV) and large hole binding energy have limited the

43   practical applications due to the low efficiency in utilizing solar energy and high rate of

44   electron-hole recombination [9, 10]. For the sake of driving the metal oxide

45   semiconductors to be sensitive toward visible light irradiation with high electron-hole pair

46   separation efficiency, considerable attentions have been paid to the construction of

47   heterosturctures or hybrids by assembling the semiconductors with designed materials,

48   such as metals, metal oxides and carbon nanomaterials [11-14]. As for ZnO, although

2

49 metal doping has been proved to be able to improve the photocatalytic activity, the

50 transition efficiency is still limited due to its inherent light absorption property [15].

51 Constructing heterojunctions by coupling ZnO with other metal oxides may present an

52 alternative method to enhance the photocatalytic efficiency, due to the feasibility of charge

53 transfer and separation through the junctions at interfaces and the interfacial defect sites

54 that act as catalytic "hot spots" [16, 17]. However, it remains a challenge to construct

55 highly effective semiconductor heterostructures with a fine homogeneity of the

56 composites.

57   Interestingly, layered double hydroxides (LDHs), which are known as anionic clays

58 with brucite-like layered structures that can be represented by the general formula

59 $[M^{II}_{1-x}M^{III}_x(OH)_2]^{x+} (A^{n-})_{x/n} \cdot mH_2O$, have been deemed to be one of the most promising

60 precursors to prepare crystallized mixed metal oxides (MMO) through calcination

61 treatment [18-21]. The pre-arrangement of metal cations in the LDH structure results in

62 the uniform distribution of the metal oxides in the calcined compounds, which can bring

63 forth an unexpected and highly improved catalytic performance of the composites [18].

64 The derivative mixed metal oxides have been employed as catalysts in varied redox

65 reactions to transform organic pollutants [20, 21]. Recently, Zn-containing LDHs have

66 been extensively explored as catalyst precursors on account of the advanced catalytic

67 activity of the derived mixed metal oxides [18, 22]. In our laboratory [23], we have found

68 that ZnAlTi- mixed metal oxides deriving from the LDH precursor can be used as

69 effective photocatalysts in the degradation of dye under solar light irradiation.

70   Carbon nanotubes (CNTs), a member of carbon nanomaterials with a cylindrical

71 sp^2-hybridized graphitic framework, have been recognized as ideal catalyst supports to

72 disperse and immobilize active materials, because of their exceptional properties [24, 25].

73 For instance, the large specific surface area of the network structure can provide more

74 exposure of active sites for facilitating the dispersion of metal oxides [26]. Besides, the

75 extraordinary electrical conductivity of the continuous network can inevitably lead to

76 highly improved charge transfer efficiency, associated with the accelerated catalytic

77 reactions [27, 28]. As documented previously, the nanohybrids by coupling carbon

78 nanomaterials with active materials presented a synergetic combination of the distinct

3

79   properties of each component in the heterogeneous catalysis systems [29, 30]. Recent

80   studies in our laboratory have demonstrated the superiorities of using carbon

81   nanomaterials as supports to anchor metal oxides for catalytic degradation of organic

82   pollutants [27, 31]. The results revealed that the sp^2-hybridized and zigzag carbons in the

83   graphene layers played vital roles in facilitating the catalytic redox reactions in aqueous

84   solutions. Moreover, it is due to the inert surface of nanocarbon materials that allows

85   limited binding sites to immobilize guest materials and thus generally leads to poor

86   dispersion and severe agglomeration of the active components, many attempts have been

87   carried out with particular emphasis upon the surface functionalization of such materials

88   [29, 32]. It was reported that the functionalization process could inevitably introduce

89   defects into the graphene lattice that resulted in increased number of oxygen species

90   adsorbed on the active sites and thus presumably improved the catalytic performance [33].

91   In this study, we first focused on combining the superiorities of functionalized CNTs

92   with ZnCr-LDHs to fabricate LDH-CNTs nanocomposites via a facile co-precipitation

93   method. The nanohybrids of CNTs and mixed metal oxides (MMO-CNTs) were derived

94   from the composite precursors of LDH-CNTs upon vacuum calcination. The

95   photocatalytic behaviors of MMO-CNTs nanohybrids were investigated for the

96   degradation of bisphenol A (BPA) under solar light irradiation. Particular attention was

97   paid to the physicochemical and optical properties of the obtained nanohybrids. Further

98   investigation was underway to probe into the role of CNTs in the nanohybrids and the

99   photocatalytic mechanism, which to our knowledge has not been published in the previous

100   works.

101   **2. Experimental methods**

102   **2.1 Preparation of photocatalysts**

103   Pristine muti-walled CNTs with an outer diameter of < 8 nm, inner diameter of 2-5

104   nm and a length of 0.5-2 mm, were acid-treated with a mixture of concentrated HNO_3 and

105   H_2SO_4 (v : v = 1 : 3) by refluxing for 4 h according to the previous literature [27]. The

106   product was recovered by filtration, washing and vacuum drying to obtain the

107   functionalized CNTs, namely A-CNTs. The nanocomposite precursors LDH-CNTs were

108   synthesized through a homogeneous co-precipitation method. 20 mg of above A-CNTs

109 were suspended in deionized water by ultrasonication for 4 h, then certain amounts of

110 $Zn(NO_3)_2 \cdot 6H_2O$ and $Cr(NO_3)_3 \cdot 9H_2O$ with Zn/Cr ratio of 2 were dissolved in the above

111 suspension to obtain a mixed solution, which was then titrated dropwise by a mixed alkali

112 solution containing NaOH and Na_2CO_3 until the solution pH reached 6.5-7.0. After that,

113 the slurry was aged in a water bath at 65 °C for 24 h. The resulting slurry was then filtered,

114 washed with distilled water and absolute ethanol alternately and dried at 60 °C, yielding

115 the LDH-CNTs-x (x = 0.02, 0.05, 0.10, 0.20) precursors, where x signified the weight

116 ratio of CNTs to LDH. The as-synthesized LDH-CNTs-x were calcined at 700 °C for 3 h

117 in vacuum to obtain the final products, which were denoted as MMO-CNTs-x. The

118 synthesis of pristine MMO was carried out under identical conditions apart from the

119 coupling of CNTs.

120 **2.2 Characterization**

121 The X-ray diffraction (XRD) patterns of the samples were recorded on a D/MAX-III

122 A X-ray diffractometer (Rigaku Ltd., Japan) by using a nickel-filtered Cu Kα radiation

123 source. The morphologies were observed using a ZEISS Merlin (SEM, Carl Zeiss,

124 Germany) field-emission scanning electron microscope and a JEM-3010 transmission

125 electron microscope (TEM, JEOL Ltd., Japan). The determination of specific surface areas

126 and pore size distributions were obtained by N_2 adsorption/desorption isotherm analysis

127 on a ASAP-2010 Chemi-sorption Surface Area Analyzer (Micrometritics, America).

128 Raman spectra were conducted on a InVia raman spectrometer (Renishaw). The X-ray

129 photoelectron spectra (XPS) were measured by a AES430S X-ray photoelectron

130 spectrometer (ANELVA, Japan) and the binding energy was referred to the C 1S peak,

131 located at 284.6 eV. Solid-state UV-vis diffuse reflection spectra (UV-vis DRS) were

132 obtained using a UV-2440 spectrophotometer (Shimadzu, Japan) equipped with an

133 integrating sphere attachment, and $BaSO_4$ was used as the reference. Photoluminescence

134 spectra (PL) measurements were performed on a F-7000 fluorescence spectrophotometer

135 (Hitachi, Japan). For the sake of evaluating the stability of the samples, the leaching

136 amounts of zinc and chromium after reactions were determined by a zeeman atomic

137 absorption spectrometer (Hitachi, Z-2000).

138 **2.3 Photocatalytic tests**

139   The photocatalytic activities of the samples were evaluated by degrading 10 mg L^{-1}

140   BPA solution under irradiation utilizing a 300 W Xe arc lamp (GXH-GXZ, 100 V, 3 A).

141   Typically, 0.125 g of photocatalyst was dispersed in 250 mL of BPA solution (10 mg L^{-1}).

142   The reaction mixture was vigorously agitated for 30 min in dark to obtain the

143   adsorption/desorption equilibrium. Then the suspension was exposed to light irradiation

144   and the concentration of BPA at given time intervals was monitored by a L-2000 high

145   performance liquid chromatography (Hitachi, Japan) equipped with a Polar-RP 80 column

146   (Synergi 4u, 250 × 4.6 mm) and a HP UV detector. The detection wavelength was selected

147   as 276 nm. The mobile phase was composed of water and acetonitrile (v/v, 50/50) at a

148   flow rate of 1.0 mL min^{-1}. To determine the radical species formed during the

149   photocatalytic degradation process, three sets of quenching experiments were carried out

150   by the addition of p-benzoquinone (BZQ), tert-butanol (TBA) and disodium

151   ethylenediaminetetraacetate (Na_2-EDTA) into the BPA solution to obtain a fixed

152   concentration.

153   **2.4 Electrochemical measurements**

154   The electrochemical properties of the samples were investigated on a CHI 600D

155   workstation (Chenhua Instruments, Co., Shanghai) with a three-electrode system, in which

156   an Ag/AgCl and a platinum foil were used as the reference and counter electrode,

157   respectively. The as-prepared samples were fixed to the glassy carbon electrode to serve as

158   the working electrode by the following steps: 2 mg of samples was ultrasonically

159   dispersed in a mixed solution containing 1 mL of ethanol and 10 μL of nafion emulsion,

160   10 μL of which was then coated on the glassy carbon disk and air-dried at ambient

161   temperature. The electrochemical impedance spectroscopy (EIS) investigations were

162   carried out in 0.1 M KCl electrolyte solution by using a 5.0 mM redox probe composed of

163    $K_3[Fe(CN)_6]$ and $K_4[Fe(CN)_6]$. The EIS data were obtained at AC amplitude of 5 mV over

164   the frequency range from 1 MHz to 0.01 Hz at 0.2 V. For the photocurrent measurement

165   (I-t), 0.2 M Na_2SO_4 solution was used as the electrolyte and the initial voltage was set as

166   -0.6 V.

167   **3. Results and discussion**

168   **3.1 Enhanced Photocatalytic Activity**

169   The photocatalytic activities of the MMO-CNTs nanohybrids were evaluated by the

170   degradation of BPA aqueous solution under simulative solar light irradiation. Note that the

171   photocatalytic decomposition of BPA could not be stimulated in the absence of light

172   illumination or any catalyst. The photocatalytic activity of the as-prepared nanohybrids

173   shows a dependence on the loading amount of A-CNTs. As shown in Fig. 1a, a remarkable

174   increase of degradation efficiency of BPA can be clearly observed for the MMO-CNTs

175   nanohybrids, compared with pristine MMO. The photocatalytic activity of the

176   MMO-CNTs nanohybrids increases gradually as the loading amount of A-CNTs increases,

177   demonstrating the superiority of MMO-CNTs hybrid nanostructures. Particularly, the

178   photocatalytic degradation efficiency of BPA after 200 min on the sample hybridized with

179   10 wt.% of CNTs (MMO-CNTs-0.10) is as high as ~100%. However, the decreased

180   photocatalytic performance for MMO-CNTs-0.20 may be ascribed to the excessive

181   amount of opaque CNTs that lead to increased absorbance and scattering of photons [1]. In

182   addition, the photodegradation process of BPA was kinetically fitted to the

183   pseudo-first-order reaction, and the much larger apparent reaction rate constants (k_a) for

184   the MMO-CNTs nanohybrids can be clearly seen in Fig. 1b. The evaluated apparent rate

185   constant reaches the highest value of 0.0265 min^{-1} for MMO-CNTs-0.10 sample, which

186   exceeds that of pristine MMO by ~2 times (k_a = 0.0086 min^{-1}). The increased k_a indicates

187   that the photocatalytic activity of MMO nanoparticales can be significantly improved by

188   the hybridization of CNTs, and the optimal loading amount of CNTs in the nanohybrids is

189   suggested to be 10 wt.%.

190   **3.2 Structural and morphological characterizations**

191   The XRD patterns of the LDH-CNTs samples and the derivative MMO-CNTs

192   samples are shown in Fig. 2. It can be seen that all the LDH-containing samples display

193   the characteristic reflections corresponding to two-dimensional hydrotalcite-like structure

194   with a hexagonal lattice and R-3m symmetry [34, 35]. Two reflections at 25.7° and 43.2°

195   observed for A-CNTs can be indexed to the intense (002) plane and (101) plane of

196   graphite layers, respectively (JCPDS no. 41-1487) [27]. However, no typical reflections of

197   A-CNTs can be distinguished within the curves of LDH-CNTs samples, proving that

198   A-CNTs are well incorporated into the hydrotalcite network [32, 36]. Comparing with that

199 of pristine LDH, the broadening reflections as the amount of hybridized CNTs increases

200 obviously indicate a reduction of particle size and crystallinity for LDH phase in the

201 LDH-CNTs hybrids (Fig. S1), which may be ascribed to the orientation/confinement

202 impact of A-CNTs on the growth of LDH nuclei [32, 36, 37]. More specifically, structural

203 defects may be introduced into LDH nanosheets with the coupling of A-CNTs, because of

204 the modified nucleation circumstances or possibly induced curvature [27, 38]. The

205 structural data of the samples are given in Table 1. It can be found that the basal spacing

206 (d_{003}) of LDH-CNTs characterized as 0.779 nm shows a slight increase in comparison to

207 that of pristine LDH $(d_{003} = 0.755$ nm), which may be attributed to the intimate interaction

208 between the brucite-like nanosheets and A-CNTs that gives rise to the weakened

209 electrostatic interaction between the positively charged laminates and the charge-balancing

210 interlayer species (CO_3^{2-}) [32, 37]. Correspondingly, the average crystallite sizes of LDH

211 phase in the nanocomposites, as calculated by Scherrer's equation [37], are in the

212 nanoscale range of 12-16 nm which are smaller than that of pristine LDH. After

213 calcination, the hydrotalcite-like structure was destroyed to form well crystallized mixed

214 metal oxides, as all the newly appearing reflections are found to be perfectly indexed as

215 the hexagonal wurtzite ZnO (JCPDS Card # 36-1451) and cubic $ZnCr_2O_4$ spinel (JCPDS

216 Card # 22-1107). Moreover, the weaker reflection intensities of MMO-CNTs than that of

217 pristine MMO indicate the smaller particle sizes and lower crystallinity of the MMO

218 phase.

219 The morphology and microstructure of the samples were investigated by SEM and

220 TEM. Fig. 3 comparatively exemplifies the SEM images of LDH, MMO, LDH-CNTs and

221 MMO-CNTs. It can be found that pristine LDH shows a typical platelet-like morphology,

222 while the LDH platelets in the LDH-CNTs hybrids are morphologically disordered and

223 dimensionally reduced, signifying a breakage or fracture of the platelets during the

224 self-assembly process of exfoliated nanosheets [38]. Here, the self-assembly of LDH

225 nuclei deposited onto A-CNTs surface to form a nanohybrid structure is mainly attributed

226 to the interaction between the positively-charged LDH platelets and negatively-charged

227 CNTs [32, 38]. Moreover, it can be observed that the introduced A-CNTs are well

228 incorporated into the sheet-shaped LDH networks. The insufficient number of defect sites,

229   especially for the nanohybrids with low loadings of A-CNTs, endows A-CNTs to be

230   wrapped up in the LDH crystallites. The pristine MMO presents the morphology of

231   uniform-sized nanoparticles due to the dehydration and decomposition of carbonate ions

232   that result in the collapse of the layered structure. For MMO-CNTs sample, it shows that

233   A-CNTs can be homogenously dispersed on a large number of nanoparticles, which can be

234   further confirmed by the typical TEM micrographs (Fig. 4). As is shown, MMO-CNTs

235   hybrids reveal the uniform sizes of about 3-5 nm, which are much smaller than that of

236   MMO (~15 nm). The intact crystalline structure and interfacial feature of ZnO and

237    $ZnCr_2O_4$ for MMO can be clearly seen in the HRTEM image. For comparison, the

238   elementary composition of LDH and LDH-CNTs was particularly investigated by EDX

239   spectra, and the corresponding data is shown in Table 2. The relative content of C and O

240   exhibits an increase with the introduction of A-CNTs, while the molar ratio of elemental

241   Zn to Cr decreases slightly, revealing that the nucleation of LDH was influenced by

242   A-CNTs.

243   Fig. 5 shows the Raman spectra of A-CNTs, pristine MMO, LDHs-CNTs and

244   MMO-CNTs nanohybrids for comparison. All the CNTs-containing samples present two

245   intense peaks at around 1322 and 1574 cm^{-1}, which can be indexed to the D and G band of

246   carbon materials, respectively, demonstrating that A-CNTs have been well incorporated in

247   both LDHs-CNTs and MMO-CNTs hybrids. It is well known that the D band is

248   characteristic of the degree of conjugation disruption in the hexagonal graphite lattice and

249   the G band is associated with the presence of sp^2-bonded carbon atoms in the tubular

250   structure [39]. The value of I_D/I_G, which is commonly used for evaluating the

251   graphitization degree and the average size of sp^2 domains in carbon materials, is calculated

252   as 0.43 for A-CNTs, indicative of a high graphitization. An intense increase of I_D/I_G for

253   MMO-CNTs-0.10 (I_D/I_G, 1.31) and LDH-CNTs-0.10 (I_D/I_G, 1.22) reveals a revocation of

254   sp^2 domains, demonstrating the successful consumption of oxygen-containing groups on

255   the outer shells of CNTs due to in-situ decoration of LDH nuclei or mixed metal oxides

256   [40]. Upon calcination, lower crystalline order of graphite phase occurred due to the

257   slightly higher I_D/I_G value of MMO-CNTs than that of LDH-CNTs. Additionally, four

258   other peaks observed in the spectrum of MMO-CNTs can be assigned to the Raman-active

259   modes of wurtzite ZnO (325 and 428 cm^{-1}) [41] and ZnCr$_2$O$_4$ spinel (509 and 673 cm^{-1})

260   [42, 43], implying the successful integration of metal oxides upon A-CNTs.

261   To get further insight into the chemical composition and bonds configuration of the

262   synthesized samples, XPS analysis was carried out and the results are presented in Fig. 6.

263   Core spectra of Zn 2p, Cr 2p, C 1s and O 1s can be clearly identified from the XPS survey

264   (Fig. 6a). As for A-CNTs, five peaks arose from the deconvolution of the C 1s core

265   spectrum can be assigned to the sp^2 graphitized carbon (284.2 eV), C-O group (285.1 eV),

266   C-OH/C=O group (286.1 eV), C-O-C/C=O group (287.1 eV) and the O=C-O group (289.0

267   eV) [44]. The intensity of the peaks that are assigned to C-O group and C-OH/C=O group

268   suggests a considerable oxidation degree in the graphite lattice of A-CNTs. The typical

269   signal of sp^2 graphitized carbon (284.8 eV) in the C 1s spectrum of MMO-CNTs-0.10

270   nanohybrid further demonstrates the integration of MMO and A-CNTs, which is consistent

271   with the above results. Besides, a dramatic change for the high-resolution XPS spectra of

272   Zn 2p can also be observed for MMO before and after their hybridization with A-CNTs,

273   implying the formation of chemical bonds at the interface of A-CNTs and MMO. For pure

274   MMO, the asymmetric peaks of Zn 2p$_{3/2}$ and Zn 2p$_{1/2}$ are located at 1020.6 and 1043.9 eV,

275   respectively. However, the corresponding peaks are centered at 1021.8 and 1044.8 eV for

276   the MMO-CNTs-0.10 nanohybrids. A similar case is observed for Cr 2p XPS spectra, only

277   the positive BE shift is relatively slight for the MMO-CNTs-0.10 nanohybrids comparing

278   with MMO. Noticeably, the chemical valence, chemical circumstances and distribution

279   status of elements can be connected with BE shift and the decrease of electron density can

280   lead to the increase of BE value [45]. As a result, the charge transfer from MMO to

281   A-CNTs surface at the interface of the hybridized nanostructure should be responsible for

282   the positive BE shift of Zn 2p and Cr 2p. This phenomenon has also been found in other

283   CNTs-based composites reported in the previous literature [37]. It is suggested that the

284   intimate interaction facilitates the charge transfer of the nanohybrid structure.

285   The textural properties of the samples were investigated by N$_2$ adsorption/desorption

286   measurements (Fig. 7) and the corresponding data are summarized in Table 1. It can be

287   observed that all the samples present type IV isotherm with a thin hysteresis loop of H3

288   type appearing at relatively high pressures, which is associated with slit-shape capillaries

289 due to the aggregates of metal oxides particles [15, 20]. This behavior is frequently

290 characteristic of mesoporous materials with three-dimensional interconnected pore

291 geometry that can be confirmed by the corresponding pore size distribution curves. The

292 much more apparent hysteresis loop on the isotherms of the samples with increased

293 A-CNTs contents is indicative of increased porosity of the materials. With the introduction

294 of A-CNTs into the nanohybrids, the BET specific surface area of the samples increases

295 sharply from 13.98 m^2 g^{-1} to 67.85 m^2 g^{-1} and the pore volume increases from 0.15 cm^3 g^{-1}

296 to 0.25 cm^3 g^{-1}, as depicted in Table 1. Note that the decreased pore volume for sample

297 MMO-CNTs-0.02 with low loading amount of A-CNTs is possibly due to the stacked

298 structure of irregular particles in the hybrids. In addition, the MMO-CNTs samples exhibit

299 a narrower pore size distribution centered at 2~40 nm than pristine MMO, which can be

300 reasonably explained by the introduced inner pores of A-CNTs [27]. This finding clearly

301 demonstrates that the loaded A-CNTs in the nanohybrids makes possible the inhibited

302 aggregation of the particles and thus give rise to more exposure of active sites in the

303 present system.

304   The optical properties of MMO-CNTs with different loading amount of A-CNTs were

305 investigated by UV-vis diffuse reflectance spectra, as depicted in Fig. 8. It is well known

306 that blank ZnO can only absorb in the UV region because of its large band gap energy. In

307 present work, the absorption in the visible light region for pristine MMO is attributed to

308 the existence of $ZnCr_2O_4$ spinel, which absorbs over the whole solar spectrum [46, 47].

309 For the case of $ZnCr_2O_4$, the transfer occurs predominantly because of the photoexcitation

310 of O 2p to Cr-$3dt_{2g}$ (~420 nm) in an octahedral environment and Cr-$3dt_{2g}$ to Cr-$3d_{eg}$ (~570

311 nm) corresponding to the d-d transition of Cr^{3+} [47, 48]. With the hybridization of A-CNTs,

312 the MMO-CNTs samples exhibit the same absorption edge with that of pristine MMO.

313 The band gap energy of the MMO-CNTs samples barely shows no change due to the fact

314 that CNTs in the hybrid structure can be characterized as free graphitic carbon. More

315 interestingly, the MMO-CNTs nanohybrids display broad absorption bands with highly

316 enhanced absorbance in the visible light region, which shows a positive correlation with

317 the increasing content of A-CNTs in the hybrid nanostructures. It is, accordingly,

318 suggested that introduced A-CNTs may lead to an increase of surface charge on metal

11

319   oxides in the nanohybrids, further affecting the fundamental generation of electron-hole

320   pairs under irradiation. As a result, the modifications of charge transfer presumably

321   contribute to the higher photocatalytic efficiency of MMO-CNTs nanohybrids.

322   **3.3 Role of CNTs in enhancing charge transfer efficiency**

323   It has been well-established that the interfacial charge transfer, which is closely

324   relevant to the probability of recombination of electron-hole pairs, is the key factor that

325   affecting the photocatalytic activities of photocatalysts [49]. To this end, EIS, transient

326   photocurrent, and PL measurements were carried out to figure out the influence of CNTs

327   on the interfacial charge transfer efficiency of the MMO-CNTs nanohybrids.

328   The EIS measurements were employed to investigate the interfacial charge transfer

329   behaviors of the prepared samples. As can be seen in the EIS Nyquist plots (Fig. 9a), the

330   semicircle radius of MMO-CNTs-0.10 is much smaller that of pristine MMO. It is

331   noteworthy that the smaller semicircle radius corresponds to a smaller charge transfer

332   resistance, which can provide evidence for the higher separation efficiency of

333   photogenerated charge carriers and faster interfacial charge transfer from MMO to

334   A-CNTs [36]. In this regard, the presence of A-CNTs with superior electrical conductivity

335   is significant to maintain high capacity during the repeated conversion reactions.

336   Fig. 9b illustrates the transient photocurrent tests for the photoactive materials over

337   repeated on/off cycles. The prompt and reproducible photocurrent response originated

338   from intermittent visible light irradiation implies the rapid charge separation and

339   recombination within the photocatalyst. It is well known that the photocurrent response is

340   closely related to the separation efficiency of photogenerated charge carriers within the

341   materials [49]. As for MMO-CNTs-0.10, the much higher photocurrent density than that of

342   MMO testifies the higher charge separation efficiency and longer lifetime of

343   photogenerated electrons and holes [11], which can be attributed to the intimate contact at

344   the interface between A-CNTs and MMO nanoparticles.

345   The recombination process of photogenerated charge carriers dependent upon the

346   charge separation efficiency can be further demonstrated by PL emission spectra. It is well

347   known that the lower recombination rate of photogenerated electron-hole pairs

348   corresponds to the lower PL intensity [50]. PL signals for MMO and MMO-CNTs-0.10

349   under excitation at around 300 nm are depicted in Fig. 9c. The significantly diminished PL

350   intensity for MMO-CNTs-0.10 nanohybrid as compared to pristine MMO indicates a

351   reduced recombination rate of photogenerated electron-hole pairs, which further confirms

352   the benefit of A-CNTs in promoting charge transfer within the obtained hybrids.

353   **3.4 Photocatalytic Mechanism Investigation**

354   At photocatalyst interface, free electrons and active holes can react with adsorbed O_2

355   and H_2O to produce $O_2^-\bullet$ and $\bullet OH$ radicals, respectively, both of which are possibly

356   responsible for the photocatalytic degradation of BPA. To reveal the photocatalytic

357   mechanism in the present system, the electron spin resonance (ESR) spin-trap technique

358   was employed and the signals of trapping the predominant reactive oxygen species are

359   depicted in Fig. 10. Both the signals of DMPO-$\bullet OH$ and DMPO-$O_2^-\bullet$ can be clearly

360   detected when pristine MMO and MMO-CNTs-0.10 dispersions are under irradiation. In

361   Fig. 10a, four characteristic peaks of DMPO-$\bullet OH$ emerge in MMO and MMO-CNTs-0.10

362   aqueous dispersions under visible light irradiation, respectively. Interestingly, the signal

363   intensities of $\bullet OH$ radicals for MMO-CNTs-0.10 nanohybrid are slightly weaker than

364   those for MMO. However, the characteristic peaks corresponding to $O_2^-\bullet$ radicals (Fig.

365   10b) detected for MMO-CNTs-0.10 nanohybrid are much stronger than that of MMO. The

366   ESR results demonstrate that both $\bullet OH$ and $O_2^-\bullet$ radicals are generated on the surface of

367   MMO-CNTs-0.10 nanohybrid in the present system, with $O_2^-\bullet$ radicals presumably as the

368   predominant reactive species. Furthermore, the quenching experiment for BPA

369   degradation with the introduction of reactive species scavengers was performed, as shown

370   in Fig. 11. The photocatalytic degradation efficiency of BPA over MMO-CNTs-0.10

371   nanohybrid was slightly reduced with the presence of tert-butanol (TBA, $\bullet OH$ scavenger).

372   However, the addition of 5 mM benzoquinone (BZQ, $O_2^-\bullet$ radical scavenger) caused an

373   obvious decrease from almost 100% to 29% in 200 min. Notably, the presence of

374   Na_2-EDTA as holes scavenger in the same system led to a fast deactivation of the

375   MMO-CNTs-0.10 photocatalyst. It is, accordingly, speculated that $O_2^-\bullet$ oxidation

376   combined with direct hole oxidation dominate the photocatalytic degradation of BPA,

377   while $\bullet OH$ oxidation also contribute to the photocatalytic process to some degree.

378   Based on the results described above, the key role of A-CNTs played in enhancing

13

379   the photocatalytic activity of MMO-CNTs nanohybrids can be attributed to three main

380   respects: firstly, the nanohybrids with higher specific surface area provide more active

381   sites for adsorption of organics and photocatalytic reactions; secondly, the extremely

382   extended absorbance in visible light region caused by A-CNTs introduction has an

383   influence on the fundamental generation of electron-hole pairs under irradiation; last, the

384   intimate interaction between MMO and conductive A-CNTs can lead to a elimination of

385   potential barrier at the grain boundaries between MMO and A-CNTs, resulting in highly

386   efficient separation of electron-hole pairs and thus more reactive oxygen species

387   participating in the degradation of BPA. More specifically, the specific π-conjugated

388   structure and outstanding electrical conductivity endow A-CNTs with rapid charge

389   transportation, through which the photoexcited electrons can be transported from MMO to

390   A-CNTs. Note that the huge π-π network of CNTs can serve as a sink for the photoexcited

391   electrons because charge transfer from the ZnO conduction band (CB) (E_{CB} = -0.5 V vs

392   NHE) to the CNTs conduction band ($E_{CB} \geq$ -0.3 V vs NHE) is energetically feasible [51,

393   52]. In addition, within the heterostructure of ZnO (E_g = 3.37 eV) and $ZnCr_2O_4$ (E_g ~ 1.5

394   eV), the potentials of CB and VB of ZnO are more negatively charged than that of

395    $ZnCr_2O_4$ [11, 46]. Because of the wide band gap, ZnO cannot be excited by visible light

396   irradiation. However, ZnO in contact with $ZnCr_2O_4$ can act as electron acceptor favoring

397   the electron-hole separation, because of the relatively higher CB bottom of $ZnCr_2O_4$ than

398   that of ZnO [29]. The schematic illustration of charge transfer process in the MMO-CNTs

399   nanohybrid structure can be exemplified in Scheme 1.

400   **3.5 Photocatalyst stability**

401   Since MMO originated from hydrotalcite-like precursor generally suffers from

402   memory effect and possible photocorrosion that inhibit the photocatalytic activity for

403   practical applications [11], it is of great significance to probe the photostability of the

404   MMO-CNTs nanohybrids. As shown in Fig. 12, it can be found that MMO-CNTs is

405   photochemically stable under irradiation in the present system in view of the negligible

406   change of photocatalytic performance, even though the photocatalyst has gone through

407   four successive recycles. The slight decrease of BPA degradation efficiency may be

408   attributed to trace leaching of metals from the catalysts during the degradation process

409   [21]. The leaching amount of zinc and chromium was detected with respective as <0.01

410   mg·L^{-1} and 0.571 mg·L^{-1} at neutral pH. Furthermore, the outstanding photostability of the

411   hybrid nanostructure can also be testified by XRD patterns (Fig. S2) of the used and fresh

412   samples, taking the intact crystalline phase into account [11]. It is speculated that trace

413   metal leaching has little effect on the crystalline structure of the nanohybrid.

414   **4. Conclusions**

415   In conclusion, the MMO-CNTs nanohybrids have been successfully synthesized via a

416   facile precursor route. The resulting MMO-CNTs nanohybrids exhibit highly enhanced

417   photocatalytic performance and cycling stability, as compared to pristine MMO. This

418   finding can be attributable to the heterostructure of ZnO and $ZnCr_2O_4$ spinel that provides

419   a synergistic effect of multi-component metal oxides for such nanohybrids and the

420   introduction of A-CNTs that facilitates the effective separation of photogenerated

421   electron-hole pairs. The as-prepared MMO-CNTs nanohybrids can serve as a promising

422   candidate for the photocatalyst materials for further applications in wastewater treatment

423   utilizing solar light.

424

430

431   **References**

432   [1] T. Xu, L. Zhang, H. Cheng, Y. Zhu, Significantly enhanced photocatalytic performance

433   of ZnO via graphene hybridization and the mechanism study, Appl. Catal., B, 101 (2011)

434   382-387.

435   [2] S. Song, B. Cheng, N. Wu, A. Meng, S. Cao, J. Yu, Structure effect of graphene on the

436   photocatalytic performance of plasmonic Ag/Ag_2CO_3-rGO for photocatalytic elimination

437   of pollutants, Applied Catalysis B: Environmental, 181 (2016) 71-78.

438   [3] B.M. Rajbongshi, S.K. Samdarshi, Cobalt-doped zincblende-wurtzite mixed-phase

439 ZnO photocatalyst nanoparticles with high activity in visible spectrum, Appl. Catal., B,

440 144 (2014) 435-441.

441 [4] Y. Lv, C. Pan, X. Ma, R. Zong, X. Bai, Y. Zhu, Production of visible activity and UV

442 performance enhancement of ZnO photocatalyst via vacuum deoxidation, Appl. Catal., B,

443 138 (2013) 26-32.

444 [5] X. Wan, X. Liang, C. Zhang, X. Li, W. Liang, H. Xu, S. Lan, S. Tie, Morphology

445 controlled syntheses of Cu-doped ZnO, tubular Zn(Cu)O and Ag decorated tubular

446 Zn(Cu)O microcrystals for photocatalysis, Chem. Eng. J., 272 (2015) 58-68.

447 [6] G. Wang, F. Wu, X. Zhang, M. Luo, N. Deng, Enhanced TiO_2 photocatalytic

448 degradation of bisphenol E by beta-cyclodextrin in suspended solutions, J. Hazard. Mater.,

449 133 (2006) 85-91.

450 [7] Y. Yang, J. Wen, J. Wei, R. Xiong, J. Shi, C. Pan, Polypyrrole-Decorated Ag-TiO_2

451 Nanofibers Exhibiting Enhanced Photocatalytic Activity under Visible-Light Illumination,

452 ACS Appl. Mater. Inter., 5 (2013) 6201-6207.

453 [8] M. Zhu, C. Zhai, L. Qiu, C. Lu, A.S. Paton, Y. Du, M.C. Goh, New Method to

454 Synthesize S-Doped TiO_2 with Stable and Highly Efficient Photocatalytic Performance

455 under Indoor Sunlight Irradiation, ACS Sustain. Chem. Eng., 3 (2015) 3123-3129.

456 [9] X. Lu, Z. Liu, Y. Zhu, L. Jiang, Sonochemical synthesis and photocatalytic property of

457 zinc oxide nanoparticles doped with magnesium(II), Mater. Res. Bull., 46 (2011)

458 1638-1641.

459 [10] H. Moussa, E. Girot, K. Mozet, H. Alem, G. Medjahdi, R. Schneider, ZnO

460 rods/reduced graphene oxide composites prepared via a solvothermal reaction for efficient

461 sunlight-driven photocatalysis, Appl. Catal., B, 185 (2016) 11-21.

462 [11] F.X. Xiao, Construction of Highly Ordered ZnO-TiO_2 Nanotube Arrays (ZnO/TNTs)

463 Heterostructure for Photocatalytic Application, ACS Appl. Mater. Inter., 4 (2012)

464 7054-7062.

465 [12] Y.J. Xu, Y. Zhuang, X. Fu, New Insight for Enhanced Photocatalytic Activity of TiO_2

466 by Doping Carbon Nanotubes: A Case Study on Degradation of Benzene and Methyl

467 Orange, J. Phys. Chem. C, 114 (2010) 2669-2676.

468 [13] L. Li, B. Cheng, Y. Wang, J. Yu, Enhanced photocatalytic H_2-production activity of

469   bicomponent NiO/TiO_2 composite nanofibers, J. Colloid Interface Sci, 449 (2015)

470   115-121.

471   [14] X. Zhang, Q. Wang, L.H. Zou, J.W. You, Facile fabrication of titanium

472   dioxide/fullerene nanocomposite and its enhanced visible photocatalytic activity, J.

473   Colloid Interface Sci, 466 (2016) 56-61.

474   [15] G. Fan, H. Wang, X. Xiang, F. Li, Co–Al mixed metal oxides/carbon nanotubes

475   nanocomposite prepared via a precursor route and enhanced catalytic property, J. Solid

476   State Chem., 197 (2013) 14-22.

477   [16] Y. Yao, G. Li, S. Ciston, R.M. Lueptow, K.A. Gray, Photoreactive TiO_2/carbon

478   nanotube composites: synthesis and reactivity, Environ. Sci. Technol., 42 (2008)

479   4952-4957.

480   [17] H. Liu, Y. Hu, X. He, H. Jia, X. Liu, B. Xu, In-situ anion exchange fabrication of

481   porous ZnO/ZnSe heterostructural microspheres with enhanced visible light photocatalytic

482   activity, J. Alloys Compd., 650 (2015) 633-640.

483   [18] X. Xiang, L. Xie, Z. Li, F. Li, Ternary $MgO/ZnO/In_2O_3$ heterostructured

484   photocatalysts derived from a layered precursor and visible-light-induced photocatalytic

485   activity, Chem. Eng. J., 221 (2013) 222-229.

486   [19] G. Mendoza-Damian, F. Tzompantzi, A. Mantilla, A. Barrera, L. Lartundo-Rojas,

487   Photocatalytic degradation of 2,4-dichlorophenol with MgAlTi mixed oxides catalysts

488   obtained from layered double hydroxides, J. Hazard. Mater., 263 (2013) 67-72.

489   [20] J. Prince, F. Tzompantzi, G. Mendoza-Damian, F. Hernandez-Beltran, J.S. Valente,

490   Photocatalytic degradation of phenol by semiconducting mixed oxides derived from

491   Zn(Ga)Al layered double hydroxides, Appl. Catal., B, 163 (2015) 352-360.

492   [21] W. Li, P.X. Wu, Y.J. Zhu, Z.J. Huang, Y.H. Lu, Y.W. Li, Z. Dang, N.W. Zhu, Catalytic

493   degradation of bisphenol A by CoMnAl mixed metal oxides catalyzed peroxymonosulfate:

494   Performance and mechanism, Chem. Eng. J., 279 (2015) 93-102.

495   [22] D. Carriazo, M. del Arco, E. Garcia-Lopez, G. Marci, C. Martin, L. Palmisano, V.

496   Rives, Zn,Al hydrotalcites calcined at different temperatures: Preparation, characterization

497   and photocatalytic activity in gas-solid regime, J. Mol. Catal. A: Chem., 342-43 (2011)

498   83-90.

499   [23] X. Wang, P. Wu, Z. Huang, N. Zhu, J. Wu, P. Li, Z. Dang, Solar photocatalytic

500   degradation of methylene blue by mixed metal oxide catalysts derived from ZnAlTi

501   layered double hydroxides, Appl. Clay. Sci., 95 (2014) 95-103.

502   [24] D. Wang, G. Yang, Q. Ma, M. Wu, Y. Tan, Y. Yoneyama, N. Tsubaki, Confinement

503   Effect of Carbon Nanotubes: Copper Nanoparticles Filled Carbon Nanotubes for

504   Hydrogenation of Methyl Acetate, ACS Catalysis, 2 (2012) 1958-1966.

505   [25] W. Chen, X. Pan, X. Bao, Tuning of redox properties of iron and iron oxides via

506   encapsulation within carbon nanotubes, J. Am. Chem. Soc., 129 (2007) 7421-7426.

507   [26] W.D. Zhang, B. Xu, L.C. Jiang, Functional hybrid materials based on carbon

508   nanotubes and metal oxides, J. Mater. Chem., 20 (2010) 6383-6391.

509   [27] W. Li, P. Wu, S. Yang, Y. Zhu, C. Kang, L.T. Tran, B. Zeng, 3D hierarchical

510   honeycomb structured MWCNTs coupled with CoMnAl-LDO: fabrication and application

511   for ultrafast catalytic degradation of bisphenol A, RSC Advances, 5 (2015) 8859-8867.

512   [28] F. Khodam, Z. Rezvani, A.R. Amani-Ghadim, Fabrication of a novel

513   ZnO/MMO/CNT nanohybrid derived from multi-cationic layered double hydroxide for

514   photocatalytic degradation of azo dye under visible light, RSC Advances, 5 (2015)

515   19675-19685.

516   [29] M. Lan, G. Fan, W. Sun, F. Li, Synthesis of hybrid Zn–Al–In mixed metal

517   oxides/carbon nanotubes composite and enhanced visible-light-induced photocatalytic

518   performance, Appl. Surf. Sci., 282 (2013) 937-946.

519   [30] G. Li, Y. Lu, C. Lu, M. Zhu, C. Zhai, Y. Du, P. Yang, Efficient catalytic ozonation of

520   bisphenol-A over reduced graphene oxide modified sea urchin-like α-MnO$_2$ architectures,

521   J. Hazard. Mater., 294 (2015) 201-208.

522   [31] Z. Huang, P. Wu, B. Gong, Y. Fang, N. Zhu, Fabrication and photocatalytic properties

523   of a visible-light responsive nanohybrid based on self-assembly of carboxyl graphene and

524   ZnAl layered double hydroxides, J. Mater. Chem. A, 2 (2014) 5534-5540.

525   [32] Y. Juan, Y. Chang, F. Xiaoming, L. Zheng, Q. Jieshan, Y. Gogotsi, Facile fabrication

526   of MWCNT-doped NiCoAl-layered double hydroxide nanosheets with enhanced

527   electrochemical performances, J. Mater. Chem. A, 1 (2013) 1963-1968.

528   [33] S. Song, H. Yang, R. Rao, H. Liu, A. Zhang, Defects of multi-walled carbon

529   nanotubes as active sites for benzene hydroxylation to phenol in the presence of H_2O_2,

530   Catal. Commun., 11 (2010) 783-787.

531   [34] C. Gomes Silva, Y. Bouizi, V. Fornes, H. Garcia, Layered double hydroxides as

532   highly efficient photocatalysts for visible light oxygen generation from water, J. Am.

533   Chem. Soc., 131 (2009) 13833-13839.

534   [35] S. Pausova, J. Krysa, J. Jirkovsky, C. Forano, G. Mailhot, V. Prevot, Insight into the

535   photocatalytic activity of $ZnCr-CO_3$ LDH and derived mixed oxides, Appl. Catal., B, 170

536   (2015) 25-33.

537   [36] W. Yang, Z. Gao, J. Wang, J. Ma, M. Zhang, L. Liu, Solvothermal One-Step

538   Synthesis of Ni-Al Layered Double Hydroxide/Carbon Nanotube/Reduced Graphene

539   Oxide Sheet Ternary Nanocomposite with Ultrahigh Capacitance for Supercapacitors,

540   ACS Appl. Mater. Inter., 5 (2013) 5443-5454.

541   [37] W. Hui, X. Xu, L. Feng, Facile synthesis and novel electrocatalytic performance of

542   nanostructured Ni-Al layered double hydroxide/carbon nanotube composites, J. Mater.

543   Chem., 20 (2010) 3944-3952.

544   [38] A. Garcia-Gallastegui, D. Iruretagoyena, M. Mokhtar, A.M. Asiri, S.N. Basahel, S.A.

545   Al-Thabaiti, A.O. Alyoubi, D. Chadwick, M.S.P. Shaffer, Layered double hydroxides

546   supported on multi-walled carbon nanotubes: preparation and CO_2 adsorption

547   characteristics, J. Mater. Chem., 22 (2012) 13932-13940.

548   [39] G. Wang, J. Yang, J. Park, X. Gou, B. Wang, H. Liu, J. Yao, Facile synthesis and

549   characterization of graphene nanosheets, J. Phys. Chem. C, 112 (2008) 8192-8195.

550   [40] P. Min-Sik, S.A. Needham, W. Guo-Xiu, K. Yong-Mook, P. Jin-Soo, D. Shi-Xue, L.

551   Hua-Kun, Nanostructured SnSb/carbon nanotube composites synthesized by reductive

552   precipitation for lithium-ion batteries, Chem. Mater., 19 (2007) 2406-2410.

553   [41] X. Wang, Q. Zhang, Q. Wan, G. Dai, C. Zhou, B. Zou, Controllable ZnO

554   Architectures by Ethanolamine-Assisted Hydrothermal Reaction for Enhanced

555   Photocatalytic Activity, J. Phys. Chem. C, 115 (2011) 2769-2775.

556   [42] C. Suchomski, C. Reitz, K. Brezesinski, C. Tavares de Sousa, M. Rohnke, K.-i.

557   Iimura, J.P. Esteves de Araujo, T. Brezesinski, Structural, Optical, and Magnetic Properties

558   of Highly Ordered Mesoporous MCr_2O_4 and $MCr_{2-x}Fe_xO_4$ (M = Co, Zn) Spinel Thin Films

559   with Uniform 15 nm Diameter Pores and Tunable Nanocrystalline Domain Sizes, Chem.

560   Mater., 24 (2012) 155-165.

561   [43] Y. Chen, Z. Liu, S.P. Ringer, Z. Tong, X. Cui, Y. Chen, Selective oxidation synthesis

562   of $MnCr_2O_4$ spinel nanowires from commercial stainless steel foil, Cryst. Growth. Des., 7

563   (2007) 2279-2281.

564   [44] K. Zhang, D. Jing, C. Xing, L. Guo, Significantly improved photocatalytic hydrogen

565   production activity over $Cd_{1-x}Zn_xS$ photocatalysts prepared by a novel thermal sulfuration

566   method, Int. J. Hydrogen Energy, 32 (2007) 4685-4691.

567   [45] K.Y. Lee, M. Kim, J. Hahn, J.S. Suh, I. Lee, K. Kim, S.W. Han, Assembly of Metal

568   Nanoparticle−Carbon Nanotube Composite Materials at the Liquid/Liquid Interface,

569   Langmuir, 22 (2006) 1817-1821.

570   [46] S. Boumaza, A. Bouguelia, R. Bouarab, M. Trari, Physical and photoelectrochemical

571   studies for hydrogen photo-evolution over the spinel $ZnCr_2O_4$, Int. J. Hydrogen Energy, 34

572   (2009) 4963-4967.

573   [47] S. Naz, S.K. Durrani, M. Mehmood, M. Nadeem, Hydrothermal synthesis, structural

574   and impedance studies of nanocrystalline zinc chromite spinel oxide material, J. Saudi.

575   Chem. Soc.

576   [48] M. Lan, G. Fan, L. Yang, F. Li, Significantly Enhanced Visible-Light-Induced

577   Photocatalytic Performance of Hybrid Zn-Cr Layered Double Hydroxide/Graphene

578   Nanocomposite and the Mechanism Study, Ind. Eng. Chem. Res., 53 (2014) 12943-12952.

579   [49] Q. Huang, S. Tian, D. Zeng, X. Wang, W. Song, Y. Li, W. Xiao, C. Xie, Enhanced

580   Photocatalytic Activity of Chemically Bonded TiO_2/Graphene Composites Based on the

581   Effective Interfacial Charge Transfer through the C–Ti Bond, ACS Catalysis, 3 (2013)

582   1477-1485.

583   [50] W.-K. Jo, N. Clament Sagaya Selvam, Enhanced visible light-driven photocatalytic

584   performance of $ZnO–g-C_3N_4$ coupled with graphene oxide as a novel ternary

585   nanocomposite, J. Hazard. Mater., 299 (2015) 462-470.

586   [51] A. Kongkanand, P.V. Kamat, Electron Storage in Single Wall Carbon Nanotubes.

587   Fermi Level Equilibration in Semiconductor–SWCNT Suspensions, ACS Nano, 1 (2007)

588   13-21.

589   [52] V. Subramanian, E.E. Wolf, P.V. Kamat, Green Emission to Probe Photoinduced

590   Charging Events in ZnO–Au Nanoparticles. Charge Distribution and Fermi-Level

591   Equilibration†, J. Phys. Chem. B, 107 (2003) 7479-7485.

592

593

594

Figures

595

596
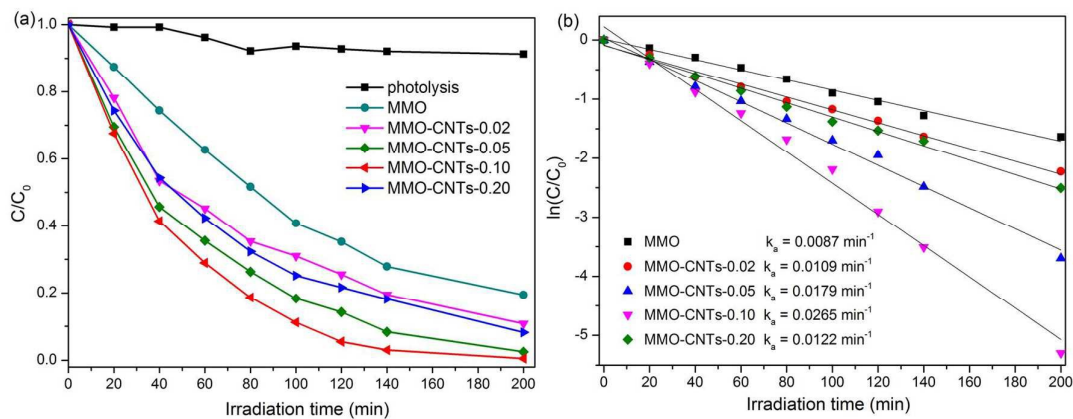
597

598 **Fig. 1** Effect of CNTs loading in MMO-CNTs nanohybrids on photocatalytic degradation of BPA
599 aqueous solution at ambient temperature (a), the pseudo-first-order kinetic for the
600 photodegradation of BPA (b). Reaction conditions: $[BPA]_0 = 10$ mg L^{-1}, catalyst dosage = 0.5 g L^{-1},
601 initial pH = 7.14.
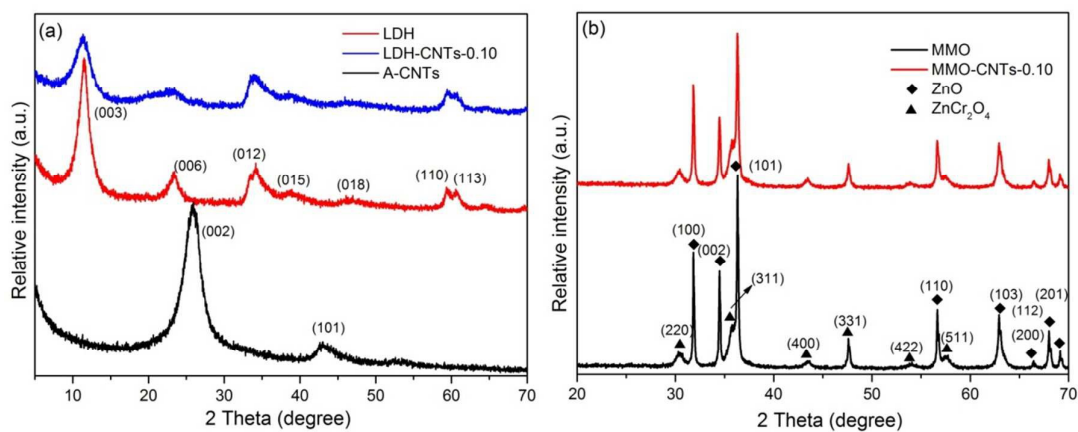
602

603 **Fig. 2** XRD patterns of LDH, LDH-CNTs and A-CNTs (a), MMO and MMO-CNTs (b)

604

605
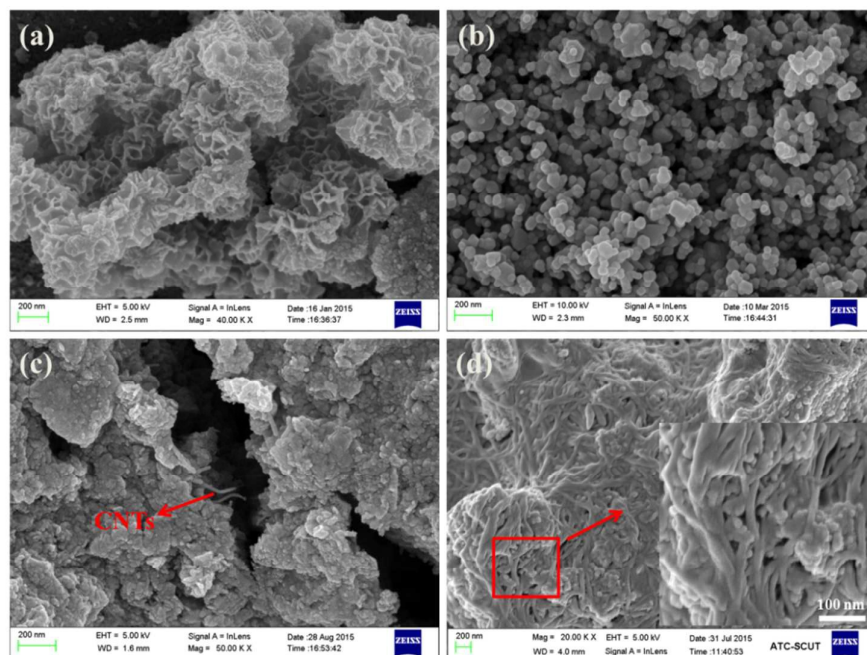
606
607   **Fig. 3** SEM images of LDH (a), MMO (b), LDH-CNTs (c) and MMO-CNTs (d)
608
609
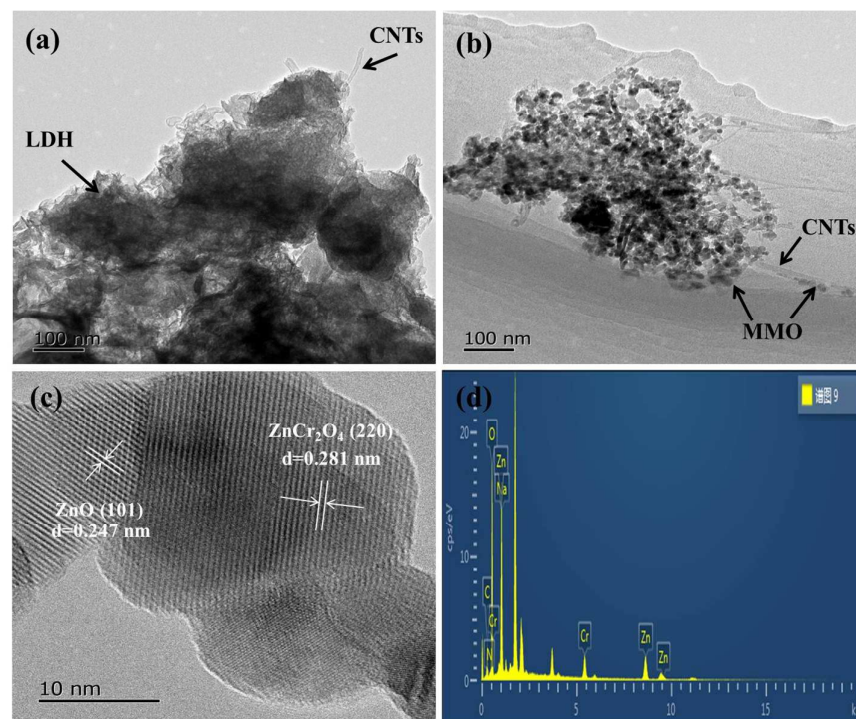
610
611   **Fig. 4** TEM images of LDH-CNTs (a), MMO-CNTs (b), HRTEM image of MMO (c) and EDX
612   spectra of MMO-CNTs

23
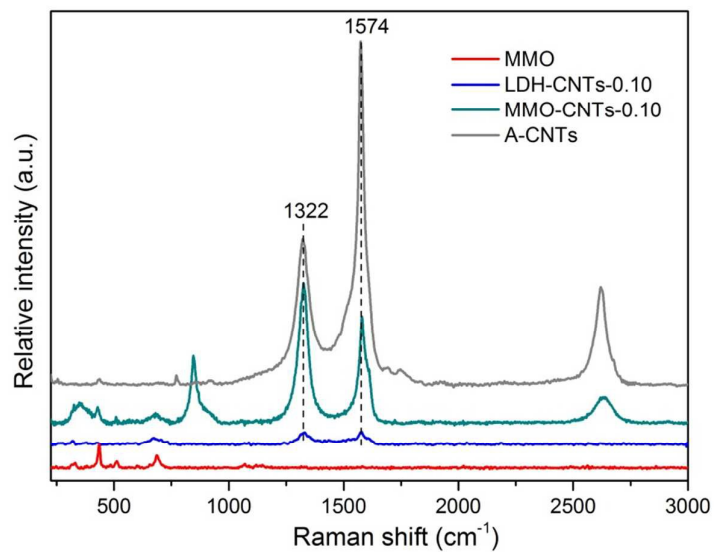
613
614   **Fig. 5** Raman spectra of A-CNTs, MMO, LDH-CNTs and MMO-CNTs
615
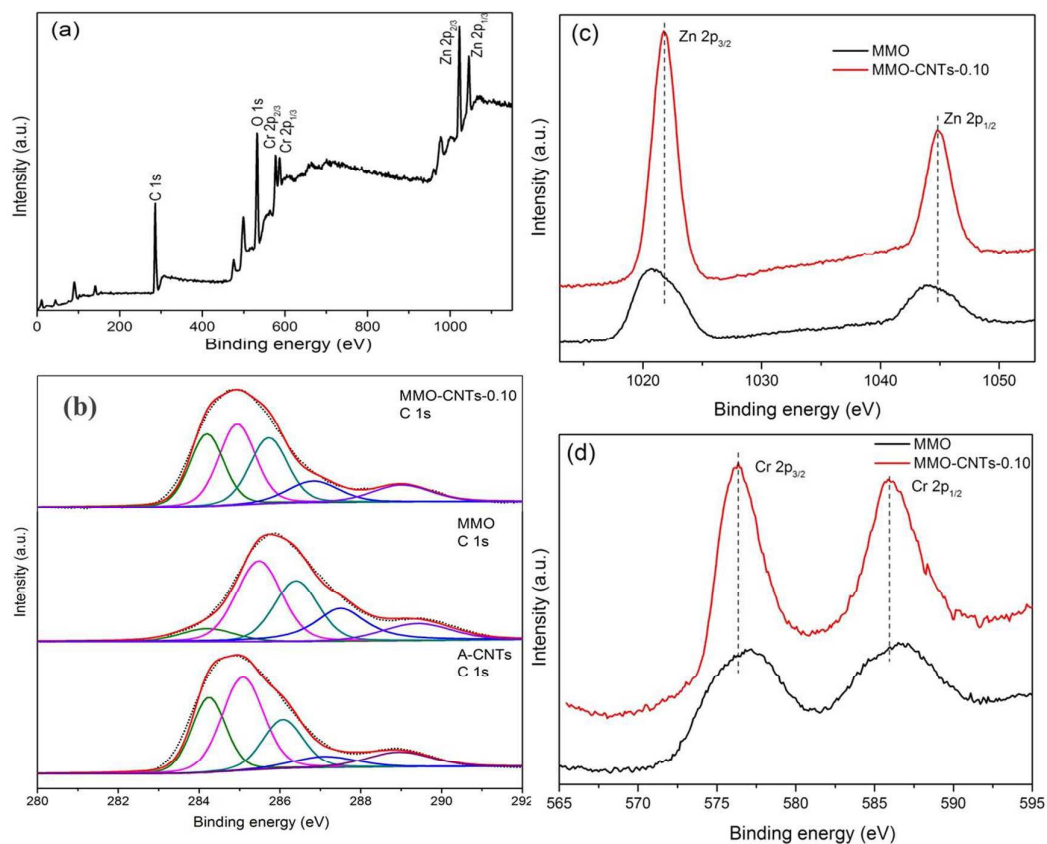
616

617   **Fig. 6** XPS survey spectra (a) of MMO-CNTs, high resolution core level spectra of C 1s (b), Zn 2p
618   (c), Cr 2p (d) for MMO and MMO-CNTs
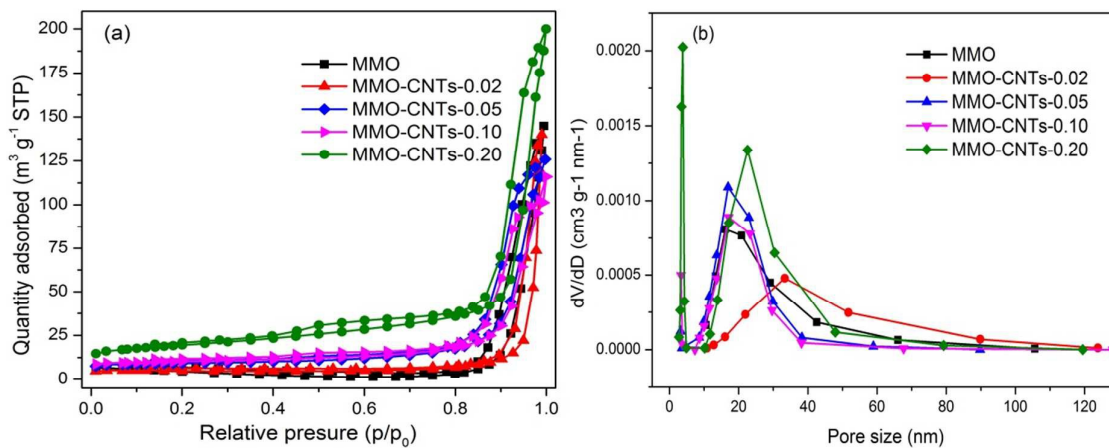
619   **Fig. 7** Nitrogen adsorption–desorption isotherms and pore size distribution curves of the obtained
620   MMO-CNTs samples

621
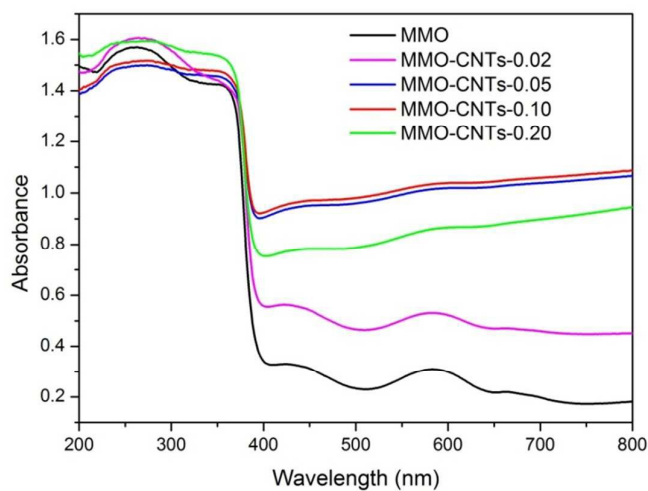
622
623   **Fig. 8** UV–vis diffuse reflectance spectra of the MMO-CNTs samples
624
625

626

627
628
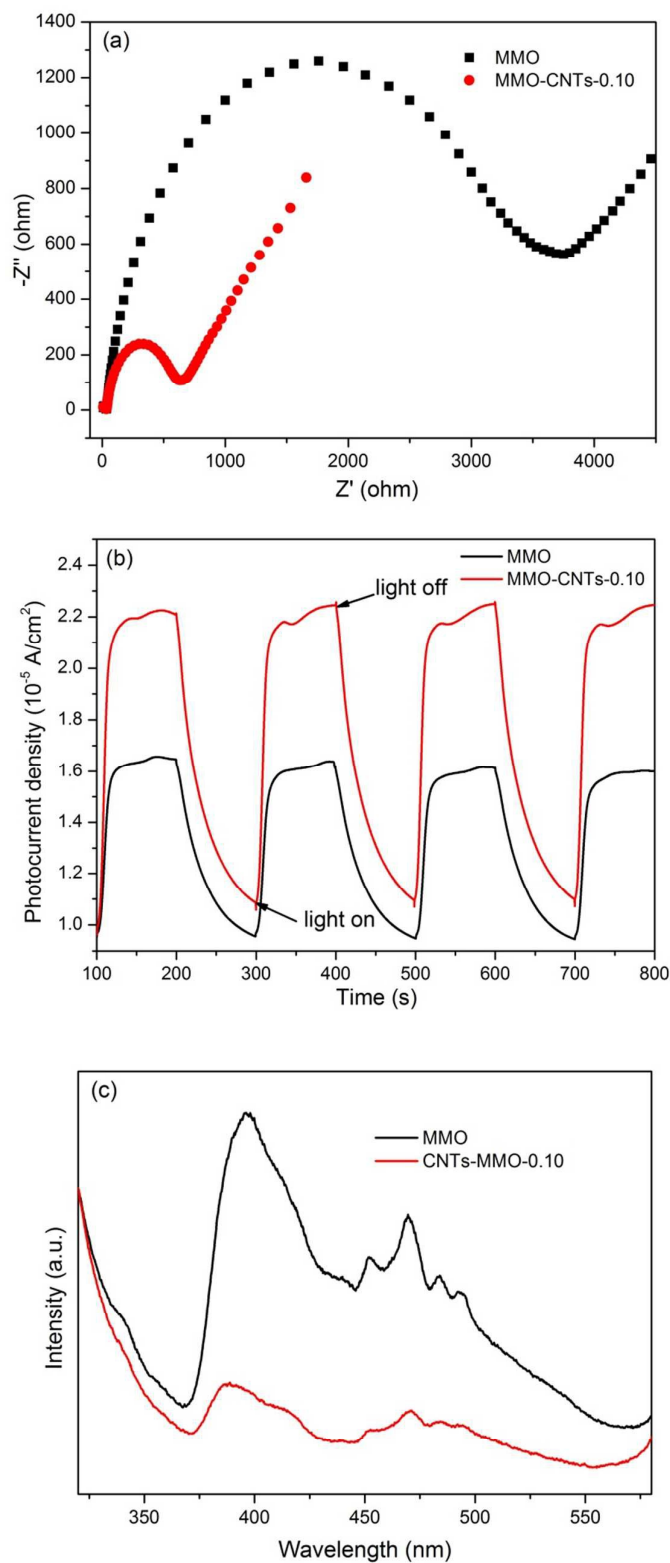
629
630   **Fig. 9** Electrochemical impedance spectroscopy (EIS) Nynquist plot (a), transient photocurrent
631   responses (b) and PL spectra (c) of MMO and MMO-CNTs-0.10
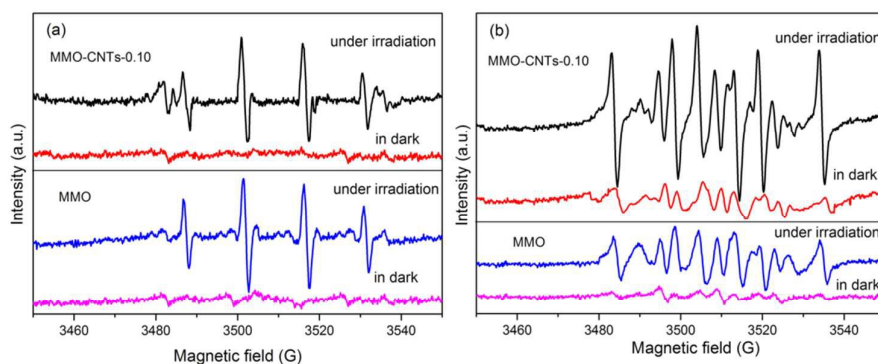
632
633   **Fig. 10** ESR spectra of radical adducts trapped by DMPO in MMO and MMO-CNTs-0.10 aqueous
634   dispersions (a) and methanol dispersions (b)
635
636
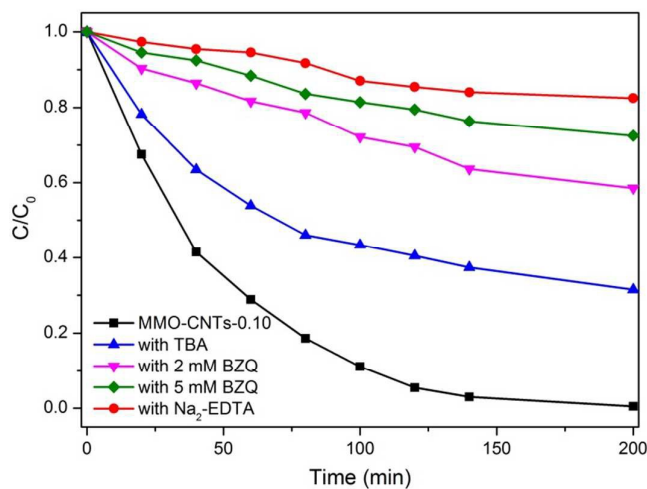
637
638   **Fig. 11** Photocatalytic degradation of BPA with the addition of hole and radical scavengers.
639   Reaction conditions: $[BPA]_0 = 10$ mg L^{-1}, catalyst dosage = 0.5 g L^{-1}, TBA and Na$_2$-EDTA dosage
640   = 2 mM.
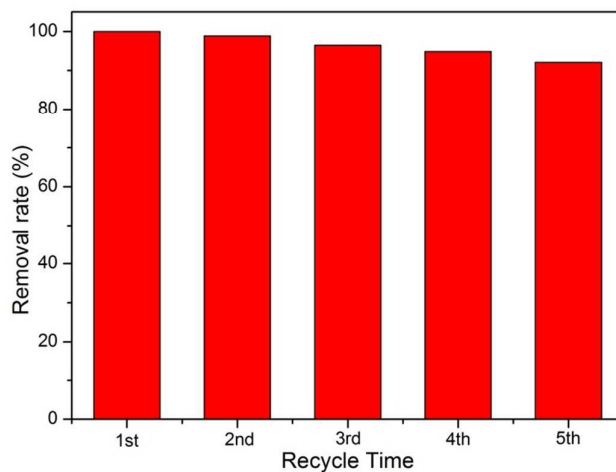
641

642   **Fig. 12** Cycling runs over MMO-CNTs-0.10 photocatalyst for degradation of BPA aqueous

643 solution at ambient temperature. Reaction conditions: $[BPA]_0 = 10$ mg L^{-1}, catalyst dosage = 0.5 g

644   L^{-1}, initial pH = 7.14.

645

646

647
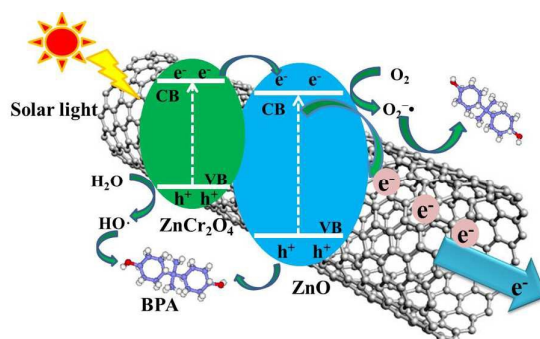
648

649   **Scheme 1.** Schematic illustration of the enhanced photocatalytic degradation of BPA by

650   MMO-CNTs nanobybrids.

651

652

653

654 # Tables

655   **Table 1.** The basal spacing (d_{003}), average crystallite size (D_e), BET surface area (S_{BET}), total pore

656   volume (V_t) and average pore size (D_p) of samples

Sample	d_{003}	D_e	Sample	S_{BET}	V_t	D_p
	nm	nm		$m^2 g^{-1}$	$cm^3 g^{-1}$	nm
LDH	0.754	14.10	MMO	13.98	0.15	42.18
LDH-CNTs-0.02	0.755	15.46	MMO-CNTs-0.02	15.97	0.08	20.28
LDH-CNTs-0.05	0.761	13.92	MMO-CNTs-0.05	31.29	0.15	20.93
LDH-CNTs-0.10	0.776	12.33	MMO-CNTs-0.10	35.15	0.16	16.79
LDH-CNTs-0.20	0.779	12.55	MMO-CNTs-0.20	67.85	0.25	14.69

657

658   **Table 2.** Chemical composition of the samples

Element	LDH		LDH-CNTs-0.10	
	wt%	Atomic %	wt%	Atomic %
C	9.79	24.47	21.89	33.11
O	19.21	37.29	44.15	52.45
Zn	51.78	25.89	24.59	9.22
Cr	19.22	12.45	9.41	5.22

659

660